Low-Frequency Motor Cortex EEG Predicts Four Rates of Force Development

Rory O'Keeffe ⑩, *Graduate Student Member, IEEE*, Seyed Yahya Shirazi ⑩, *Member, IEEE*,
Alessandro Del Vecchio ⑩, Jaime Ibáñez ⑩, Natalie Mrachacz-Kersting ⑩, *Member, IEEE*, Ramin Bighamian ⑩,
John-Ross Rizzo ⑩, Dario Farina ⑩, *Fellow, IEEE*, and S. Farokh Atashzar ⑩, *Senior Member, IEEE*

Abstract—The movement-related cortical potential (MRCP) is a low-frequency component of the electroencephalography (EEG) signal that originates from the motor cortex and surrounding cortical regions. As the MRCP reflects both the intention and execution of motor control, it has the potential to serve as a communication interface between patients and neurorehabilitation robots. In this study, we investigated the EEG signal recorded centered at the Cz electrode with the aim of decoding four rates of force development (RFD) during isometric contractions of the tibialis anterior muscle. The four levels of RFD were defined with respect to the maximum voluntary contraction (MVC) of the muscle as follows: Slow (20% MVC/s), Medium (30% MVC/s), Fast (60% MVC/s), and Ballistic (120% MVC/s). Three feature sets were assessed for describing the EEG traces in the classification process. These included: (i) *MRCP Morphological Characteristics* in the δ-band, such as timing and amplitude; (ii) *MRCP Statistical Characteristics* in the δ-band, such as standard deviation, mean, and kurtosis; and (iii) *Wideband Time-frequency Features* in the 0.1-90 Hz range. The four levels of RFD were accurately classified using a support vector machine. When utilizing the Wideband Time-frequency Features, the accuracy was $83\% \pm 9\%$ (mean $\pm$ SD). Meanwhile, when using the MRCP Statistical Characteristics, the accuracy was $78\% \pm 12\%$ (mean $\pm$ SD). The analysis of the MRCP waveform revealed that it contains highly informative data on the planning, execution, completion, and duration of the isometric dorsiflexion task. The temporal analysis emphasized the importance of the δ-band in translating to motor command, and this has promising implications for the field of neural engineering systems.

Index Terms—NeuroHaptics, force decoding, BCI.

Rory O'Keeffe and Seyed Yahya Shirazi are with the Department of Electrical and Computer Engineering, New York University (NYU), New York, NY 11201 USA.

Alessandro Del Vecchio is with the Department of Artificial Intelligence in Biomedical Engineering, Friedrich-Alexander University, 91054 Erlangen, Germany.

Jaime Ibáñez is with BSICoS Group, I3A institute, IIS Aragón, University of Zaragoza, 50009 Zaragoza, Spain.

Natalie Mrachacz-Kersting is with the Institute for Sport and Sport Science, Albert Ludwig University of Freiburg, 79085 Freiburg, Germany.

Ramin Bighamian is with the Office of Science and Engineering Laboratories, Center for Devices and Radiological Health, United States Food and Drug Administration, Silver Spring, MD 20993 USA.

John-Ross Rizzo is with the Department of Neurology, New York University School of Medicine, New York, NY 10016 USA.

Dario Farina is with the Department of Bioengineering, Imperial College London, SW7 2AZ London, U.K.

S. Farokh Atashzar is with the Department of Electrical and Computer Engineering, Department of Mechanical and Aerospace Engineering, NYU WIRELESS and NYU Center for Urban Sciences and Progress (CUSP), Brooklyn, NY 11201 USA (e-mail: f.atashzar@nyu.edu).

Digital Object Identifier 10.1109/TOH.2024.3428308

I. INTRODUCTION

MOTOR-RELATED potentials are the aggregation of neural activity in the motor cortex. The neural activity can be related to sensory integration, motor preparation, motor learning, and execution of a motor task [1], [2], [3], [4], [5], [6]. Research suggests that the dorsal premotor cortex (PMd) is pivotal in motor planning [7], [8], [9]. Additionally, the supplementary motor area (SMA) is recognized as a vital hub for integrating information from cognitive, motor, and sensory sources [10], [11]. When electroencephalography (EEG) recordings are taken from the central region of the brain, particularly near the Cz electrode location, they represent motor-related local field potentials (LFPs) in the premotor cortex, SMA, and medial motor cortex [12], [13], [14].

Motor-related potentials can discriminate motor impairments, quantify a variety of tasks and also monitor the improvements after rehabilitation, especially for stroke and other central nervous system impairments [3], [15], [16], [17]. Motor-related potentials are especially important from the human-machine interface perspective because they provide information about the sensorimotor processing which precedes motor actions [15], [18], [19]. For cue-based movements, the PMd is believed to have a major role in this pre-movement activity which can be captured as negative deflections in the motor-related potentials [20], [21].

The most noticeable characteristics of the movement-related cortical potential (MRCP) are the negative deflections in the neural trace. The MRCP is a component of the low-frequency (0–4 Hz, δ-band) EEG, which is elicited when a cued or self-paced voluntary movement is planned and executed [22], [23], [24], [25]. EEG electrodes positioned at the mid-central area of the brain, such as Cz, are used to record MRCP in response

to lower-limb movements. These electrodes predominantly reflect sources from the premotor cortex, primary motor cortex, and SMA [4], [26], [27], [28]. The MRCP comprises three components, namely the readiness potential (RP), movement-monitoring potential (MMP), and motor potential, corresponding to movement planning, control, and execution [29], [30]. The RP, also known as the Bereitschafts potential in the case of self-paced movements, is a negative deflection that may begin as early as 2 seconds before the movement onset [29], [31].

The RP consists of two phases, the second of which usually has a steeper slope and maximum amplitude over the primary motor cortex [31]. Both the RP and MMP have been shown to be related to the task's kinetic parameters, for example, force and rate of force development (RFD) [22], [29]. In response to motor imagery, an imaginary MRCP is generated, which typically has a smaller amplitude than an actual movement [29]. The MRCP has been utilized to forecast and comprehend task execution in both healthy adults and individuals with medical conditions such as Parkinson's disease, tremor, and stroke [25], [32], [33]. The existence of an MRCP in response to motor tasks such as isometric dorsiflexion has been detected with an accuracy >85% in related studies [34], [35].

For brain-computer interface (BCI) and neurorehabilitation technologies, it is crucial to map the MRCP to multiple levels of a single kinetic parameter. However, existing studies have had difficulty achieving high classification accuracy with more than two levels of a single parameter [36], [37]. Nonetheless, studies have shown that the MRCP can be detected with low latency (high temporal resolution) [35], [38]. Identifying the MRCP at various levels of a single kinetic parameter will be a significant step forward for BCI and neurorehabilitation technologies. Additionally, the MRCP can distinguish left vs. right hand, and foot movements [39], [40]. When using the MRCP to map to a kinetic parameter, distinguishing two levels of force or RFD has been successful (accuracy >74% for force, accuracy >81% for RFD) [41]. Successful classification of multiple RFD levels is particularly important as the human-machine interface (HMI) can aid the user in performing the task at the intended speed. This provides an additional motor dimension beyond the start and stop of the task and may be crucial for neurorehabilitation technologies.

Decoding multiple levels of movement intensity with MRCP features has strong potential in BCI technologies, such as assisting impaired users with task execution at the desired intensity. The aim of this study is to evaluate the capacity of EEG, in particular, δ-band MRCP features, to decode four levels of RFD during isometric ankle dorsiflexion. Our first hypothesis is that four levels of RFD can be accurately discriminated using full-band EEG features from a larger scalp area spanning nine central electrodes. Secondly, we hypothesize that the MRCP's temporal δ-band features from the Cz electrode can achieve a comparable classification accuracy.

This study investigates the potential discrimination of four RFD levels with MRCPs, comparing features both in the δ-band and in the full EEG band. Healthy subjects performed isometric ankle dorsiflexion while EEG signals were recorded. Characteristics of the MRCP that scaled in response to the RFD, such as

amplitude and timing, constituted the first feature set (the *MRCP Morphological Characteristics*, see II-E for detailed feature definitions). A second feature set was constructed from ten temporal attributes of the MRCP, such as mean and standard deviation (the *MRCP Statistical Characteristics*, see II-F for detailed feature definitions). Highlighted features from the morphological and statistical characteristics demonstrated a monotonic response to the intensity of the RFD. Some highlighted features are as follows: $\min_1$ and $\min_n$ for the morphological characteristics, slope and standard deviation in the $(0, 1)$s window for the statistical characteristics. The classification accuracy of each feature set was evaluated by using a support vector machine classifier to predict the RFD level and applying 5-fold cross-validation. A third feature set which consisted of time-frequency features in the 0.1–90 Hz band from nine electrodes of the motor cortex (the *Wideband Time-frequency Features*, see II-G for detailed feature definitions), was investigated, and the performance was used as a benchmark. The low-frequency temporal features in the MRCP Statistical Characteristics showed a relatively strong discriminative power, with an accuracy of 78%. The results highlight the role of the δ-band in translating motor command and have potential applications in HMI systems.

II. METHODS

Five healthy volunteers (aged 20-28 years), without any prior HMI experience participated in the study. All subjects gave their signed consent, which was conducted in accordance with the principles outlined in the Helsinki Declaration and approved by the University College London Department of Clinical and Movement Neurosciences (approval date: April 26th 2017, approval reference number: 10037/001).

A. Experimental Protocol

Each subject was seated in a chair with their leg constrained and ankle fixed to a pedal with an attached force transducer (NEG1, OT Bioelettronica, Torino, Italy, Fig. 1(a)). Subjects were instructed to perform a defined rate of isometric dorsiflexion of the dominant-sided (right in all subjects) ankle. Four rates of force development (RFD) were defined based on the time interval to reach a target force level of 60% of maximal voluntary contraction (MVC). With real-time visual feedback, subjects followed a triangular profile (Fig. 1(b)) from 0 to 60% MVC with the durations of: (i) 3 s, (ii) 2 s, (iii) 1 s, and (iv) 0.5 s, corresponding to RFDs of (i) 20% MVC/s (Slow), (ii) 30% MVC/s (Medium), (iii) 60% MVC/s (Fast), and (iv) 120% MVC/s (Ballistic).

Each experimental session started with measuring the maximum voluntary contraction (MVC) force so that the RFD levels could be defined. A training phase (approximately 5 min) was included to let the subjects familiarize themselves with executing the defined force profile while receiving visual feedback. Subjects were guided to execute a set of at least 25 successful isometric ankle dorsiflexion repetitions at each of the four target RFD levels. The RFD level was constant across all repetitions within a given set, and there was a 5 s resting period between each repetition [27], [43]. The sequence of the four sets corresponding
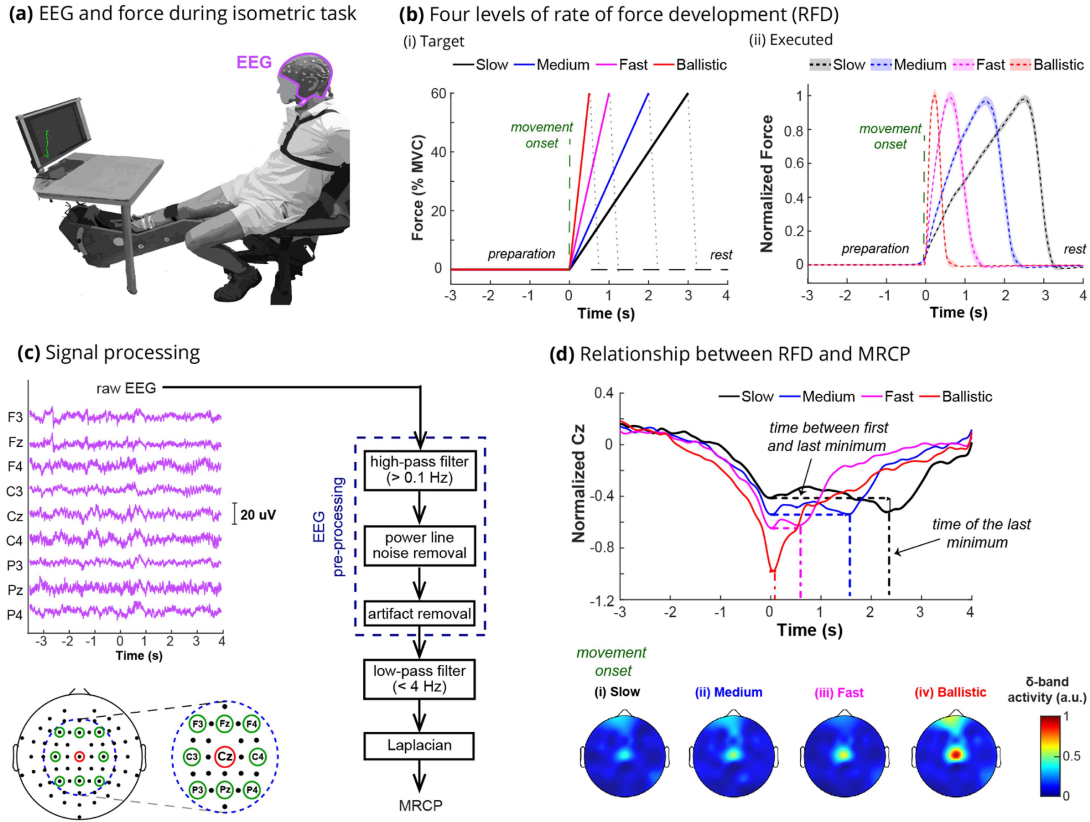
Fig. 1. (a) EEG signals were recorded from 64 electrodes, and force signals were measured using a load cell while subjects performed guided isometric ankle dorsiflexion. (b) (i) Subjects were guided to reach 60% maximum voluntary contraction (MVC) with four durations (0.5 s, 1 s, 2 s and 3 s), giving four target levels of rate of change of force (Ballistic: 120% MVC/s, Fast: 60% MVC/s, Medium: 30% MVC/s and Slow: 20% MVC/s). (ii) The mean and 95% confidence interval (CI_{95}) executed force plots are shown for each of the Slow, Medium, Fast, and Ballistic tasks. (c) EEG signals are pre-processed by applying a high-pass filter at 0.1 Hz, removing power line noise with a notch filter at 50 Hz, and removing unwanted artifacts with an ICA-based method [42]. The MRCP is produced by applying a low pass filter at 4 Hz and performing a Laplacian spatial filter with eight electrodes surrounding Cz. (d) Several MRCP morphological characteristics, such as the time features of the minima, seem to scale with the task duration. Heat maps indicate that δ-band activity is highest for Cz and scales in proportion to RFD.

to the RFD levels was randomized for each subject. Between each set, a break of 5 min was provided [27], [43]. If the study personnel observed in real-time that the executed force for a given repetition had a large deviation from the target force profile, the repetition was marked as a failure, and an extra repetition was added to the current set.

B. Data Acquisition

EEG data were wirelessly recorded from 64 electrodes assembled on an active-electrode cap (ActiChamp, Brain Products GmbH, Germany) at 1000 Hz. The 64 electrodes were arranged according to the extended 10–20 (10%) configuration [44]. The force signal was recorded at 2048 Hz from a force transducer mounted on a pedal and connected to an amplifier (Quattrocento, OTBioelettronica, Turin, Italy). At the start of each set of isometric dorsiflexions, a trigger pulse was sent to the EEG recording system when the force signal recording started, such that the EEG and force signals could be synchronized later. The movement onset was defined as the time at which the force signal reached 10% of its peak trial value (approximately 6% MVC, as in Fig. 1(b)). Using this movement onset time as 0 s for each

trial, a $(-3, 4)$s window was used to investigate the EEG signals for each trial.

C. EEG Pre-Processing

Following the recording, signals were processed using MATLAB R2022b (MathWorks Inc. Natick MA). Nine EEG electrodes of interest, including and neighboring Cz, i.e., P3, Pz, P4, C3, Cz, C4, F3, Fz, and F4, were used for the analysis (Fig. 1(c)). EEG signals from the nine electrodes were filtered with (i) a zero-phase, 2nd-order Butterworth high pass filter with a cutoff frequency of 0.1 Hz and with (ii) a zero-phase, 4th-order Butterworth band stop filter (47.5–52.5 Hz) to remove line noise. Unwanted signal artifacts were removed with an ICA-based algorithm [42].

D. MRCP Analysis

The nine pre-processed EEG signals were low-pass filtered at 4 Hz with a zero-phase, 4th-order Butterworth filter. To extract the MRCP, a Laplacian spatial filter was applied to the Cz electrode to enhance the spatial resolution (Fig. 1(c)). The mean MRCP, μ_{sam}, across all trials of all subjects was
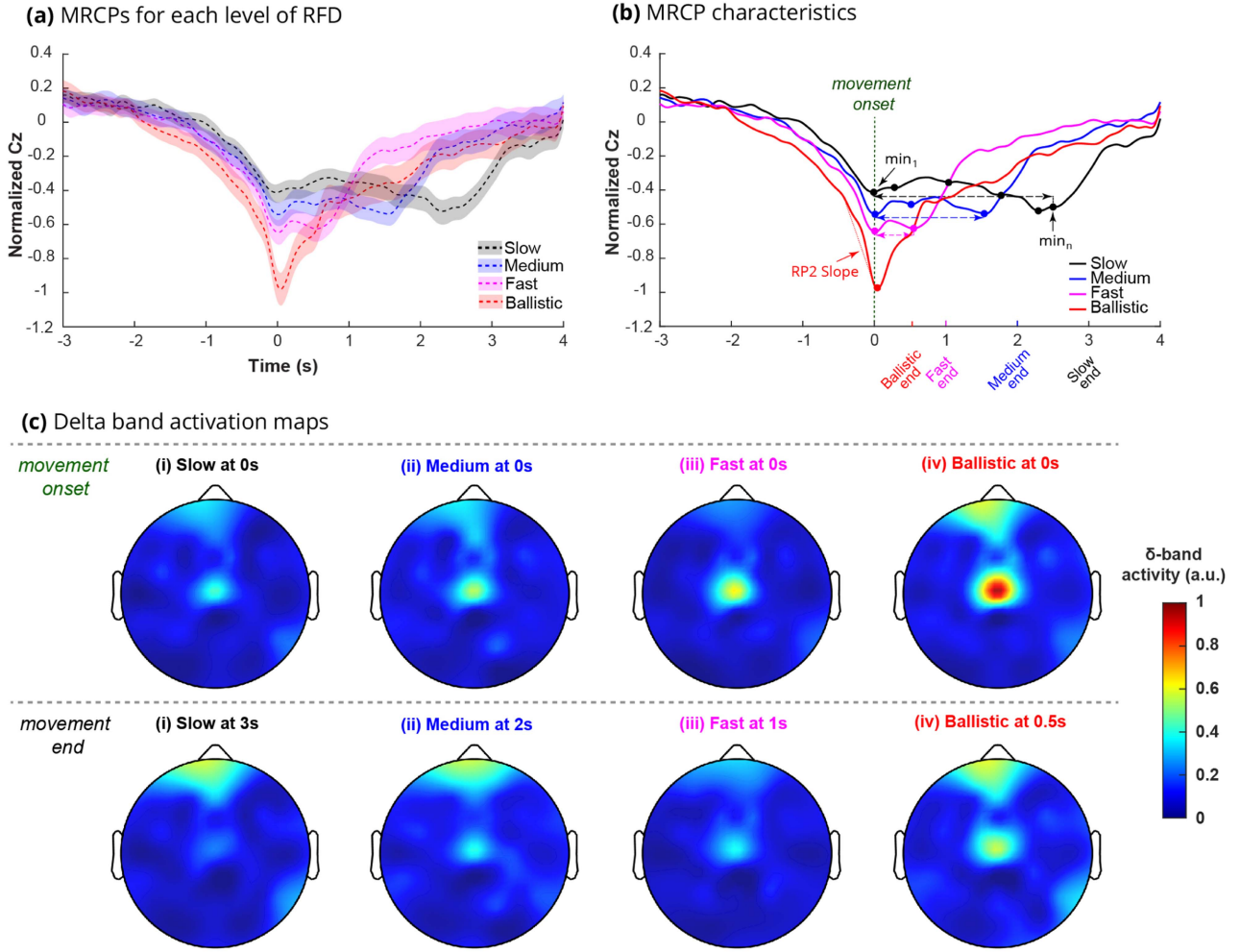
Fig. 2. (a) Mean (center line) MRCP with 95% confidence interval (shaded area) across all subjects. (b) Mean MRCP for each class of RFD, where the dots signify local minima. The first local minimum ($\min_1$) and last local minimum ($\min_n$) are indicated for the Slow RFD. The slope of the late readiness potential (RP2 slope) is indicated for the Ballistic RFD. The time between the first and last local minimum (denoted by a horizontal dashed line) is closely related to the duration of the force application. (c) Topographical plots of δ-band activation for the recorded electrodes. The maps in the top row considered the movement onset (0 s), while the maps in the bottom row considered the planned movement end as the time window center. The dominant δ-band activation appears to be at Cz and is monotonically ascending with the level of RFD (with Slow having the smallest and Ballistic having the largest). The activation of Cz trended higher at the movement onset than at the end. For each subject and trial, the median activity was quantified for the 100 ms window around the specified time. Here, the maps represent the median across all subject trials and were normalized to the maximum activity across the eight plots.

computed, for each RFD, and the results can be seen in Fig. 2(a) and (b). Additionally, the sample standard deviation, $std_{sam} = \frac{\sigma}{\sqrt{n}}$, across all trials of all subjects was computed and used to compute the MRCP's 95% confidence interval (CI_{95}, Fig. 2(a)) as $CI_{95} = \mu_{sam} \pm (Z_{95})(std_{sam}) = \mu_{sam} \pm (1.96)(std_{sam})$. The δ-band activity was plotted, resulting in the activation heat maps as explained in the following. After band-pass filtering, each of the 64 recorded electrodes was spatially filtered with an appropriate Laplacian configuration. The configuration was chosen based on the position of the electrode of interest and its surrounding electrodes such that the Euclidean distance deviation from the ideal configuration was minimized [45]. The configuration was chosen based on the position of the electrode of interest, and its surrounding electrodes [45]. The median magnitude of each electrode's time domain signal across all subject trials was computed, and the median in a 100 ms window produced a

singular value for the topographical heat maps (Fig. 2(c)). The 100 ms window was centered at the movement onset for the maps in the top row (centered at 0 s for all classes). For the bottom row, the window was centered at the planned movement end (centered at 3 s for Slow, at 2 s for Medium, at 1 s for Fast and at 0.5 s for Ballistic). Each electrode's value was normalized using the maximum across the eight plots in Fig. 2(c).

E. Feature Set 1: MRCP Morphological Characteristics

The following features were extracted from the MRCP signal at Cz, $MRCP(t)$, for each trial:

1) The RP2 slope (m_{RP2}), i.e., the slope of the MRCP signal $MRCP(t)$ between -0.5 s and 0 s [31]:

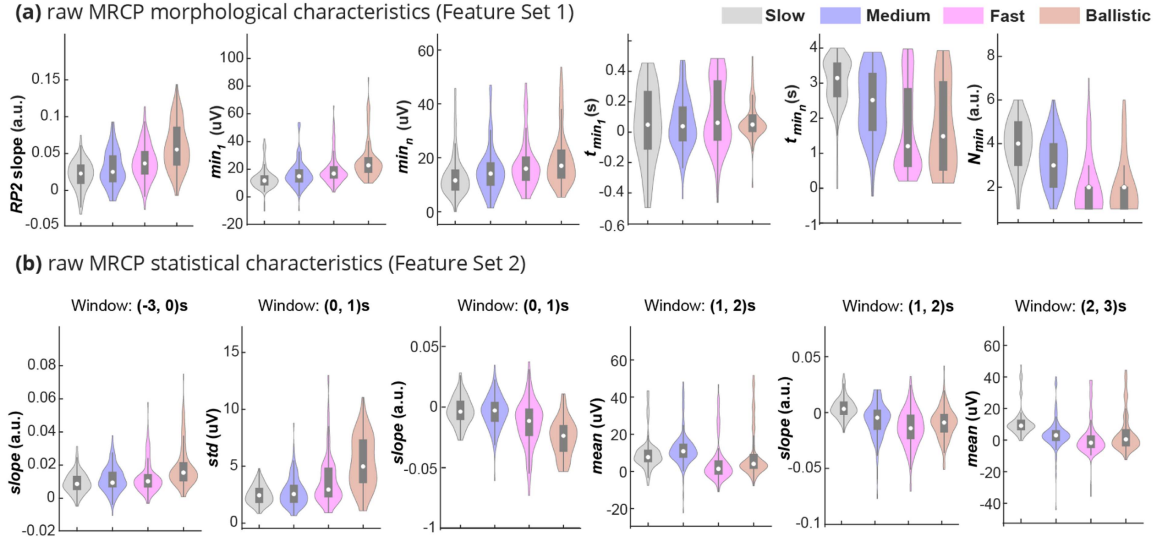$$m_{RP2} = \frac{MRCP(0) - MRCP(-0.5)}{0.5} \tag{1}$$

Fig. 3.   Violin plots of MRCP features (without rank transformation). The raw feature values for all subject trials are shown for each distribution ($n = 125$). See Section II-H for more information about how to interpret the violin plots.

2) The first local minimum's value, $\min_1$, traditionally called peak negativity (PN)
3) The time at which $\min_1$ occurred, $t_{\min_1}$
4) The number of local minima, $N_{\min}$
5) The last local minimum's value, $\min_n$
6) The time at which $\min_n$ occurred, $t_{\min_n}$.

For demonstration purposes, $\min_1$ and $\min_n$ are indicated on the mean MRCP of the Slow RFD, while RP2 slope is highlighted for the Ballistic RFD (Fig. 2(b)). The local minima, including $\min_1$ and $\min_n$, were identified for each trial by finding peaks of the inverted MRCP signal. Therefore, the *findpeaks* command in MATLAB was applied to $-MRCP(t)$ with the following parameters: (i) peak must occur within the $(-0.5, 4)$s time window (to include most extreme cases of local minima), (ii) peak height equal to at least half of global maximum, (iii) time between peaks equal to at least 0.25 s. The classification performance of the full feature set (Fig. 5) and each feature alone (Fig. 6) was investigated.

F. Feature Set 2: MRCP Statistical Characteristics

The following features were extracted from $MRCP(t)$ for the following time windows, $(-3, 0)$s, $(0, 1)$s, $(1, 2)$s, $(2, 3)$s, and $(3, 4)$s, within each trial:
1) Mean value
2) Standard deviation (std)
3) Mean absolute value
4) Trapezoidal integral (area under the curve)
5) Slope m_{if} between the initial MRCP value of the time window $MRCP(t_i)$ and the final MRCP value of the time window $MRCP(t_f)$:

$$m_{if} = \frac{MRCP(t_f) - MRCP(t_i)}{t_f - t_i} \qquad (2)$$

6) Slope sign change (SSC), which is calculated thus for a given signal $x(t)$ [46], [47]:

$$SSC = \sum_{n=2}^{N-1} f\{((x(t_n) - x(t_{n-1}))$$
$$\times ((x(t_n) - x(t_{n+1}))\}$$
$$f\{y\} = \begin{cases} 1 & \text{if y} > 0 \\ 0 & \text{otherwise} \end{cases} \qquad (3)$$

7) Mean $\frac{d}{dt}$ of MRCP signal
8) Skewness s, which gives a measurement of how asymmetrically a signal is distributed about the mean, as

$$s = E\left[\left(\frac{x - \mu}{\sigma}\right)^3\right]. \qquad (4)$$

9) Kurtosis k, which evaluates the tailedness of a distribution as given below:

$$k = E\left[\left(\frac{x - \mu}{\sigma}\right)^4\right] \qquad (5)$$

10) Shannon's entropy $H(x)$, which gives a measure of the uncertainty in a signal $x(t)$ as:

$$H(X) = -\sum P_X(X_i)log_2 P_X(X_i) \qquad (6)$$

where X denotes the discretized version of the signal and $P_X(X_i)$ denotes the distribution of X [48], [49], [50].

All features computed in each time window were included in the feature set (10 features $\times$ 5 windows = 50 features) used to train and evaluate the performance of the classifier (Fig. 7). We also evaluated the classifier performance when it was only trained on individual time windows (e.g., 1 to 2 seconds, or 3 to 4 seconds), which is depicted in Fig. 8 and Table III.
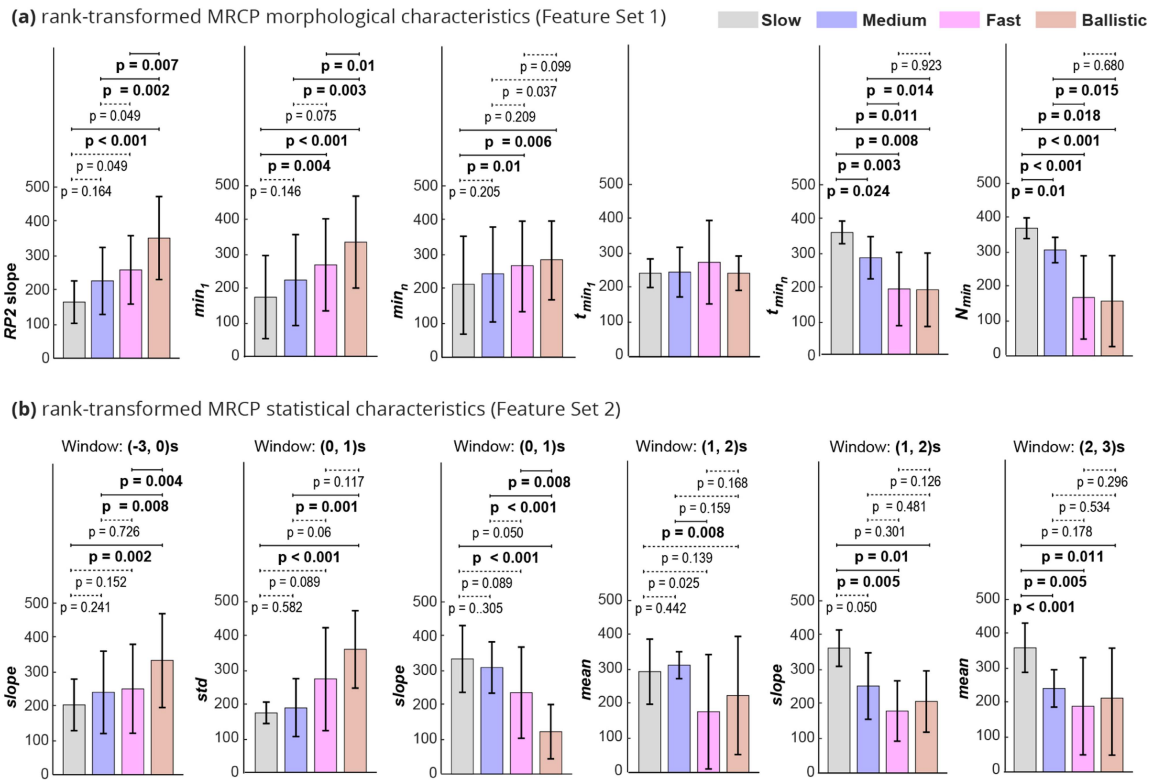
Fig. 4. Post-hoc RM-ANOVA pairwise comparisons regarding the effect of RFD level are indicated for the highlighted rank-transformed features. As five subjects conducted 25 trials at four RFD levels in our analysis, each rank-transformed feature has a value between 1 and 500 ($5 \times 25 \times 4 = 500$). The color-coded bar and associated vertical black line indicate the estimated marginal mean (EMM) and 95% confidence interval at a given RFD level. (a) The RP2 slope, min_1, and min_n showed trends of monotonical ascension, while t_{min_n} and N_{min} showed trends of monotonical descension in response to increasing RFD. Five of the six features shown demonstrated a difference between Slow and Ballistic RFD ($p < 0.009$). (b) The slope in the $(-3, 0)$s window and the std in the $(0, 1)$s window showed trends of monotonical ascension, while the slope in the $(0, 1)$s window, the slope in the $(1, 2)$s window, and the mean in the $(2, 3)$s window showed trends of monotonical descension in response to enlarging RFD. Five of the six features shown demonstrated a difference between Slow and Ballistic RFD ($p < 0.012$).
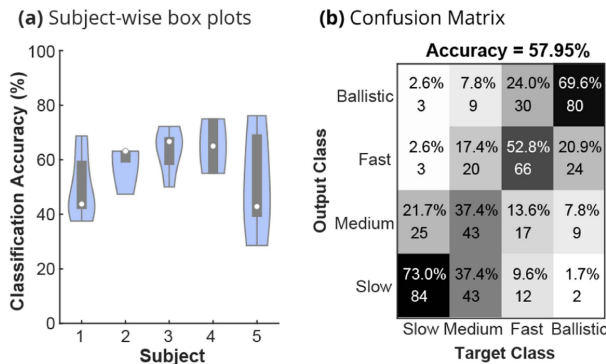

Fig. 5. Classification accuracy from the MRCP Morphological Characteristics (Feature Set 1). (a) Subject-wise violin plots of classification accuracy. The distribution of the classification accuracy across the five folds is shown for each subject. See Section II-H for more information about how to interpret the violin plots. (b) Overall confusion matrix. The classification results from all subjects are pooled, and the mean accuracy is shown above.

Fig. 6. Feature-wise classification accuracy from MRCP Morphological characteristics (Feature Set 1). Each violin plot depicts the accuracy obtained when classifying the level of RFD with the highlighted feature alone. See Section II-H for more information about how to interpret the violin plots.

G. Feature Set 3: Wideband Time-Frequency Features

The nine pre-processed EEG signals were filtered with a zero-phase, 4th-order Butterworth low-pass filter with a cut-off frequency of 90 Hz. The sh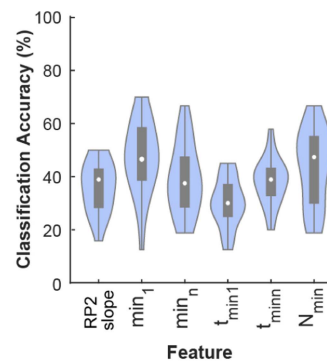ort-time Fourier transform (STFT) was performed on each trial with 50% overlapping Hamming windows of 2 s. The nine-electrode STFT formed the Wideband Time-frequency Features in the broad frequency range of interest (0.1–90 Hz).
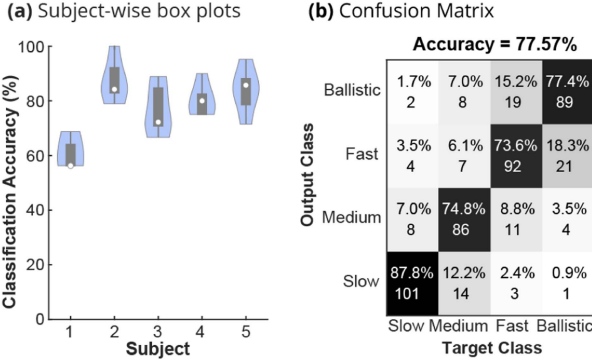
Fig. 7. Classification accuracy from the MRCP Statistical Characteristics (Feature Set 2) from all time windows. (a) Subject-wise plots of classification accuracy. The distribution of the classification accuracy across the five folds is shown for each subject. See Section II-H for more information about how to interpret the violin plots. (b) Overall confusion matrix. The classification results from all subjects are pooled and mean accuracy is shown above.
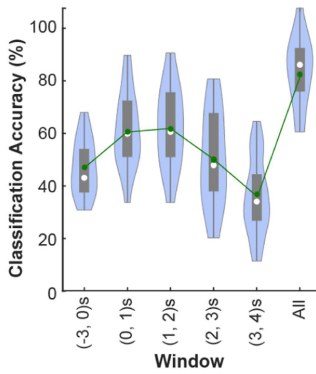

Fig. 8. Window-wise classification accuracy from statistical characteristics (Feature Set 2). Each of the first five violin plots depicts the accuracy obtained when classifying the level of rate of change of force with features across just that time window. The final violin plot shows the accuracy when classifying with features pooled from all time windows. Each violin plot shows a $subjects \times folds$ distribution for the given time window. The green line plot indicates the mean classification accuracy. See Section II-H for more information about how to interpret the violin plots.

H. Violin Plots

Note that each violin plot in this paper shows the distribution of data points as density curves. The width of each curve corresponds with the approximate frequency of data points along the y-axis. Within each violin plot, there is a box plot where the white dot indicates the median and the grey box shows the interquartile range.

I. Statistical Analysis

The relationship of features with respect to the four levels of RFD was analyzed for the MRCP Morphological Characteristics (Feature Set 1) and for the MRCP Statistical Characteristics (Feature Set 2). The feature distributions when combining all

TABLE I
RESULTS FOR THE RM-ANOVA MODEL TO TEST THE EFFECT OF RFD LEVEL ON THE MRCP MORPHOLOGICAL CHARACTERISTICS

Feature	F-statistic	Test Significance	η_p
RP2 slope	15.32	p < 0.001	0.79
min_1	17.6	p < 0.001	0.81
min_n	7.15	p = 0.005	0.64
t_{min_1}	0.358	p = 0.784	0.08
t_{min_n}	16.05	p < 0.001	0.8
N_{min}	18.21	p < 0.001	0.82

Values are shown for F-statistic, p-values, and effect size (η_p). The significance level was set at $p = 0.05$.

TABLE II
RESULTS FOR THE RM-ANOVA MODEL TO TEST THE EFFECT OF RFD LEVEL ON THE MRCP STATISTICAL CHARACTERISTICS

Feature	F-statistic	Test Significance	η_p
slope in (-3, 0)s	9.95	p < 0.001	0.71
std in (0, 1)s	11.7	p < 0.001	0.74
slope in (0, 1)s	18.88	p < 0.001	0.82
mean in (1, 2)s	5.19	p = 0.015	0.56
slope in (1, 2)s	6.51	p = 0.007	0.62
mean in (2, 3)s	12.35	p < 0.001	0.75

Values are shown for F-statistic, p-values, and effect size (η_p). The significance level was set at $p = 0.05$.

subject trials at each RFD level are shown as violin plots for Feature Set 1 and Feature Set 2 (Fig. 3). Note that each of the five subjects performed 25 trials at four RFD levels. Hence, a 2-way Repeated Measures ANOVA (RM-ANOVA) model was chosen, where the two factors were the RFD level and trial number [51], [52]. Since the normality assumption was violated by the raw feature distributions, a rank transformation was performed to ensure normality prior to conducting RM-ANOVA [53], [54]. As five subjects conducted 25 trials at four RFD levels in our analysis, the rank-transformed features have a value between 1 and 500 ($5 \times 25 \times 4 = 500$). The RM-ANOVA analysis was conducted in IBM SPSS Statistics for Windows, Version 29.0.2.0, Armonk, NY. With regard to the RM-ANOVA model assumptions, it should be noted that for all rank-transformed features: (i) normality was maintained (Shapiro-Wilk Test: $p > 0.05$), (ii) no significant outliers were observed, and (iii) sphericity (homogeneity of variances) was maintained (Mauchly's test: $p > 0.09$) [51], [55].

The significance level for the RM-ANOVA tests was $\alpha = 0.05$. It should be noted that the effect of the trial number was not significant for any of the MRCP features (RM-ANOVA: $F(24, 96) > 0.095, p > 0.96$), the effect of interaction between trial number and RFD level was not significant for any of the MRCP features (RM-ANOVA: $F(72, 288) > 0.095, p > 0.96$), and only the effect of the RFD level is reported in the Results section. The RM-ANOVA test results for the effect of RFD level, including F-statistic, p-value, and effect size (partial eta-squared, η_p) are shown in Tables I and II. If the effect of RFD level
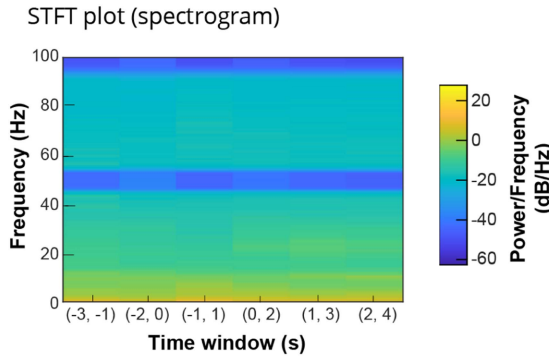
Fig. 9. An example STFT plot (spectrogram) is shown for the Cz electrode during the Ballistic task. Feature Set 3 includes STFT features from nine electrodes including Cz.
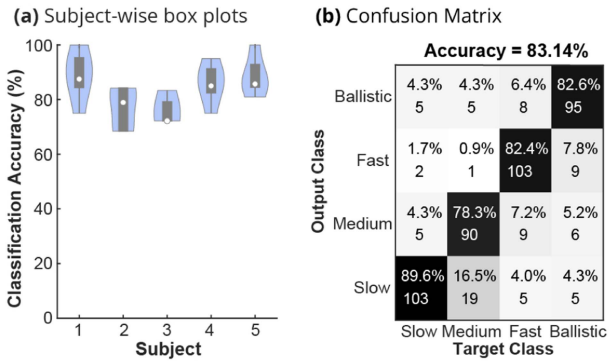

Fig. 10. Classification accuracy from wideband STFT features (Set 3) derived from the full spectrum of nine electrodes. (a) Subject-wise plots of classification accuracy. The distribution of the classification accuracy across five folds is shown for each subject. See Section II-H for more information about how to interpret the violin plots. (b) Overall confusion matrix. The classification results from all subjects are pooled and the mean accuracy is shown above.

was significant ($F(3, 12) > 3.475, p < 0.05$), post-hoc pairwise comparisons were conducted using the estimated marginal mean (EMM) (Fig. 4). The color-coded bar and associated black vertical line indicate the EMM and 95% confidence interval, respectively, at a given RFD level (Fig. 4). The significance level was adjusted for multiple comparisons using the Bonferroni-Holm procedure [56], [57], and a significant p-value is indicated with bold font and a solid line (Fig. 4).

J. Machine Learning Classification

A Support Vector Machine (SVM) classifier with a linear kernel function was used for all feature sets. For a given subject, there were 25 trials of each RFD class (Slow, Medium, Fast, Ballistic). The machine learning model was evaluated by performing k-fold cross-validation with $k = 5$ [58], [59]. The trials of each subject were divided into five distinct folds. Four folds, ~20 trials for each subject, were designated for training the classifier while the remaining fold, ~5 trials, constituted the test set. The accuracy of the trained classifier was evaluated by predicting the RFD level of each trial in the test set based on the EEG features, and comparing the prediction to the ground truth. The train and test process was repeated for each of the five folds. The distribution of the classification accuracies across the five folds of each subject is shown for Feature Set 1 in Fig. 5(a), for Feature Set 2 in Fig. 7(a), and for Feature Set 3 in Fig. 10(a). The confusion matrices in Figs. 5(b), 7(b), and 10(b) indicate the patterns of classification performance across all subject trials. The distribution of classification accuracies across all subject folds is shown for each feature in Fig. 6 and for each time window in Fig. 8.

III. RESULTS

A. Feature Set 1: MRCP Morphological Characteristics

Increases in RFD resulted in identifiable changes in the MRCP signal features. The CI_{95} plots demonstrated significant differences between the group average MRCPs across the RFDs (Fig. 2(a)). The value of the first local minimum, the distance between the first and last local minima, and the MRCP slope before the execution, i.e., the readiness potential (RP2), seemed

to be among the features contributing to the separation of the MRCPs and their respective CI_{95}. Furthermore, the distance between the first and last MRCP minima seemed to scale with the force development time for each group (Fig. 2(a) and 2(b)). The activation maps after Laplacian filter indicated monotonically increasing activity around the Cz area from the Slow, to Medium, to Fast, and to Ballistic RFDs. This activity tended to diminish at the end of the force development (Fig. 2(c)). For reference, the force development time is 3 s for the Slow group, 2 s for the Medium group, 1 s for the Fast group, and 0.5 s for the Ballistic group. The brain activity centered around Cz trended highest at the time points considered for Ballistic, particularly at the movement onset (Fig. 2(c)).

The rank-transformed MRCP Morphological Characteristics showed significant differences depending on the level of RFD for pre-movement, movement onset, and post-movement features. The effect of RFD level was significant for the following features within the rank-transformed MRCP Morphological Characteristics: RP2 slope, $\min_1$, $\min_n$, t_{min_n}, and $N_{\min}$ (RM-ANOVA: $F(3, 12) > 7.14, p < 0.006$) (Table I). The EMM of RP2 slope, $\min_1$, and $\min_n$ showed trends of monotonical ascension in response to increasing RFD level (Fig. 4(a)). The post-hoc RM-ANOVA test showed that RP2 slope and $\min_1$ were higher at the Ballistic RFD compared to the Slow, Medium, and Fast RFD levels (RP2 slope: $p < 0.008$, $\min_1$: $p < 0.011$) (Fig. 4(a)). The EMM of features with a post-movement component such as t_{min_n} and $N_{\min}$ showed trends of monotonical descension in response to increasing RFD level (Fig. 4(a)). The post-hoc pairwise comparison indicated that t_{min_n} and $N_{\min}$ were enlarged at the Slow RFD compared to the Medium, Fast, and Ballistic RFD levels (t_{min_n}: $p < 0.025$, N_{min_1}: $p < 0.011$) (Fig. 4(a)). Five of the six features shown demonstrated a difference between Slow and Ballistic RFD (post-hoc RM-ANOVA test: $p < 0.009$).

Using the MRCP Morphological Characteristics as the feature set for the SVM algorithm demonstrated medium discriminative power in relation to the four levels of RFD ($>50\%$), which is double the chance level for four classes (Fig. 5). The average

TABLE III
WINDOW-WISE CLASSIFICATION ACCURACY (CA) USING THE MRCP STATISTICAL CHARACTERISTICS

Subject/Window	(-3, 0)s	(0, 1)s	(1, 2)s	(2, 3)s	(3, 4)s	All
1	41.25+/- 8.39	46.25+/- 12.18	42.5+/- 9.27	31.25+/- 7.65	25+/- 8.84	60+/- 5.59
2	54.74+/- 7.98	72.63+/- 5.77	60+/- 16.48	47.37+/- 8.32	25.26+/- 10.12	87.37+/- 7.98
3	45.56+/- 9.13	62.22+/- 14.38	66.67+/- 11.79	33.33+/- 7.86	24.44+/- 7.45	76.67+/- 9.13
4	38.37+/- 2.74	53.26+/- 6.71	62.63+/- 8.37	54+/- 11.4	52.74+/- 4.47	80.26+/- 6.12
5	38.1+/- 8.91	49.52+/- 5.43	58.1+/- 12.33	57.1+/- 11.86	39.05+/- 8.52	83.81+/- 8.65

The mean ± SD CA across the five folds is shown subjectwise for each window.

overall accuracy was ∼58% across subjects and classes (Fig. 5). The confusion matrix for this feature set also suggested a strong discriminative power if only two RFD groups were considered (Fig. 5(b)). The cumulative accuracy of the adjacent RFD groups (i.e., Ballistic and Fast vs. Medium and Slow) reached >84%. Note that this feature set had only *six features* derived from the δ-band MRCP and robustly classified dual-level RFDs and performed well beyond the chance level for the four-level RFD classification using SVM. With regard to the feature-wise classification (Fig. 6), N_{min} and min_1 had the highest accuracy (∼45%), followed by RP2 slope and t_{min_n} (∼40%).

B. Feature Set 2: MRCP Statistical Characteristics

The rank-transformed MRCP Statistical Characteristics showed significant differences depending on the level of RFD for pre- and post-movement features. The effect of RFD level was significant for all six of the highlighted rank-transformed MRCP Statistical Characteristics (*RM-ANOVA: $F(3, 12) > 5.18, p < 0.016$*) (Table II). The EMM of the slope in the $(-3, 0)$s window showed trends of monotonical ascension in response to increasing RFD level (Fig. 4(b)). The post-hoc RM-ANOVA test indicated that the slope in the $(-3, 0)$s window was enlarged at the Ballistic RFD compared to the Slow, Medium, and Fast RFD levels ($p < 0.009$) (Fig. 4(b)). On the other hand, the EMM of the slope in the $(0, 1)$s window showed trends of monotonical descension in response to increasing RFD level (Fig. 4(b)). The post-hoc pairwise comparison illustrated that the slope in the $(0, 1)$s window and the mean in the $(2, 3)$s were higher at the Slow RFD compared to the Medium, Fast, and Ballistic RFD levels (slope in the $(0, 1)$s window: $p < 0.009$, mean in the $(2, 3)$s window: $p < 0.012$) (Fig. 4(b)). Five of the six features shown demonstrated a difference between Slow and Ballistic RFD (*post-hoc RM-ANOVA test: $p < 0.012$*).

Combining the ten MRCP statistical characteristics from each of the five time windows resulted in an RFD classification accuracy of >75% (Fig. 7). Four out of the five subjects had >75% classification accuracy (Fig. 7(a), Table III). The mean accuracy across subjects and RFD classes was ∼78% (Fig. 7(b)), with the highest discriminative accuracy at 87.8% for the Slow RFD. The cumulative accuracy of the two-level RFD with adjacent classes (i.e., Ballistic and Fast vs. Medium and Slow) reached >91% (Fig. 7(b)). Considering the MRCP Statistical Characteristics only from selected time windows as the SVM feature set reveals that the SVM classifier is likely most responsive to attributes in the $(1, 2)$s window with accuracy ∼60% (Fig. 8). The least discriminative power was for the $(3, 4)$s time window with ∼30% (around chance) accuracy. Interestingly, the median accuracy

with all the time windows included was ∼80%, which was greater than each individual time window (Fig. 8). The detailed per subject and window accuracy results also confirmed that for all subjects, either the $(0, 1)$s or the $(1, 2)$s window provided the highest accuracy (Table III).

C. Feature Set 3: Wideband Time-Frequency Features

An exemplar spectrogram plot for the STFT of one of the nine electrodes included in Feature Set 3 is shown in Fig. 9. The SVM classification using STFT full temporal and spectral feature set yielded >80% classification accuracy for the four levels of RFD. The subject-wise classification accuracy revealed >80% accuracy for four out of the five subjects (Fig. 10(a)), while the overall group accuracy for the STFT feature set was at ∼83% (Fig. 10(b)). In comparison to the wideband classification accuracy, a preliminary analysis indicated that performing the STFT on the nine electrodes filtered to the δ-band band led to a reduced classification accuracy (∼67%). Adjacent classes with the fastest RFDs (i.e., Fast and Ballistic) had a high mutual misclassification rate compared to the misclassification rate when the inter-class distance increased.

IV. DISCUSSION

A. Key Outcomes

In this paper, the ability of the MRCP to predict four levels of RFD was investigated and novel success was achieved. Four RFD levels could be discriminated with ∼78% accuracy when only using δ-band MRCP statistical characteristics. In this study, we investigated the complete MRCP waveform for four levels of RFD, which provided a rich source of information about the (i) planning, (ii) execution, (iii) completion, and (iv) duration of the isometric dorsiflexion task utilizing the tibialis anterior muscle. The results showed that morphological features, such as the time between the first and last minima encapsulate critical information with potential use in HMI. We demonstrated that both rank-transformed MRCP morphological and statistical features present monotonic trends with respect to the RFD levels (Slow RFD was differentiated from Ballistic RFD in 10 out of 12 features shown in Fig. 4, $p < 0.012$). This paper also highlights morphological features such as the number of minima (N_{min}) and the time of the last minimum (t_{min_n}) which have at least the same discriminative power as previously highlighted features such as RP2 slope and time of first minimum (min_1). Using the MRCP feature sets provides a transparent and interpretable SVM classifier that is not a "black box" and can inform researchers about the EEG waveform dynamics. The novel MRCP features

are neurophysiological indications of the underlying mechanism of motor monitoring and execution by the motor cortex and the neighboring areas. Our results illustrate the exciting possibility of MRCP to RFD mapping, which has strong potential applications, particularly in neurorehabilitation.

B. New Findings About MRCP Characteristics

Previous studies have explored the significance of certain MRCP features, such as RP2 slope and $\min_1$ [28], [60], [61], [62], [63]. However, our research indicates that other features, such as the timing of the last minimum (t_{min_n}) and the number of minima $(N_{\min})$, may have matched or superior discriminative power (Figs. 4 and 6). We observed that while $\min_1$, $\min_n$, and RP2 slope decreased in response to increasing RFD levels, $N_{\min}$ and t_{min_n} increased (Figs. 2 and 4). Previous studies have identified the local minimum of the negative deflection that occurs around the movement onset as the peak negativity (PN) [63], [64], denoted in this study as $\min_1$. The scaling of PN $(\min_1)$ may indicate the level of corrective actions and error processing in the premotor and motor cortices [13], [65]. Interestingly, we observed that the PN is not necessarily a global minimum when considering the full task duration (e.g., Slow in Fig. 2(b)). Rather, the PN is just the first of a set of local minima, indicating that the error processing and movement monitoring can continue beyond the initial recruitment of the muscle.

Depending on the task duration, there may be deeper negative deflections after the $\min_1$ point. Previous research indicated that two levels of RFD can be detected by two distinct $\min_1$ points [36]. In our study, we defined four levels of RFD by varying the duration to reach the target force (60% MVC). It was demonstrated that $\min_1$ increases in response to the RFD level (Figs. 2(a) and 4(a)). In addition, the timing of the last MRCP minimum $(\min_n)$ scaled in inverse proportion to RFD (Figs. 2(a) and 4(a)). In other experimental setups with a constant force duration rather than constant force, the amplitude rather than the timing of MRCP minima would perhaps be more discriminative regarding the RFD level. Our findings demonstrate that the timing and intensity of the MRCP minima indicate different motor activities and cortical processes [25], [66]. The minima are distinctive features of the movement monitoring potential (MMP) and are linked to the subject's intention to correct errors when tracking the force profile [29], [67].

C. Strong Discriminative Power of MRCP

The strong discriminative power of EEG features with regard to four RFD levels validated both hypotheses in the study, and shows promise for decoding the user's intention with enhanced resolution. The Wideband Time-Frequency features successfully discriminated the four RFD levels with a classification accuracy of 83% (Fig. 10), validating the first hypothesis. The MRCP Statistical Characteristics demonstrated 78% classification accuracy (Fig. 7), highlighting the role of δ-band signals in motor tasks. The four-class classification performance of $\sim 80\%$ achieved here is comparable to previous studies which only discriminated two levels of RFD [36], [41]. Even though

the full spectrum of EEG from 9 channels (9774 features) can secure a 5% higher accuracy than the performance of δ-band MRCP, the results support that the small feature set of statistical MRCP characteristics can recover the classification performance and closely follow that of the full spectrum, confirming the second hypothesis. Furthermore, the two-level classification accuracy with the MRCP Statistical Characteristics was at $\sim 90\%$ (Fig. 7(b)), suggesting strong discrimination of the behavior based on the MRCP waveform when the Ballistic and Fast trials are compared with the Slow and Medium trials.

Our preliminary analysis of applying the STFT only on the δ-band showed an overall average accuracy of 67%, underlining the advantage of the MRCP Statistical Characteristics compared to the STFT feature set of the same signal. The strong classification accuracy of MRCP Statistical Characteristics (with very low number of features) is aligned with the individual features showing statistical differences between the levels of RFD (Fig. 4(b)); for example, our analysis showed that the Slow task can be differentiated from Ballistic by the rank-transformed signal mean, slope and standard deviation features $(p < 0.012)$. The MRCP Statistical Characteristics are indicative of the complexity of the waveform and the rate and overall magnitude (and power) of the deflection of the waveform from its baseline. The combination of these statistical characteristics quantitatively describes the changes in the MRCP, and, based on the results, can effectively map the signal to the different RFD levels.

D. Significance in the Context of BCI

The results presented here show the advantageous interpretability of the MRCP features. The MRCP Statistical Characteristics and full-spectrum STFT feature sets achieved strong accuracy thresholds with a simple SVM algorithm. The use of brain-computer interfaces to decode spatial/kinematic aspects of motion in the upper limb has been extensively studied, as reflected in the literature [68], [69]. However, the literature is limited when it comes to decoding kinetic aspects of motor intention, specifically the intensity of task conduction. In recent years, some research has been conducted to predict two levels of rate of force development using EEG signals in the lower limb [36], [62]. Despite these efforts, no study has been done on discriminating more than two intensity levels. A higher number of detectable intensity levels is crucial for improving the resolution of BCI in decoding the intensity of intended motion for more intuitive implementations.

This paper presents a novel investigation about the information content of MRCP, in the context of decoding as many as four grades of intensity, which has not been reported before. In recent times, complex machine learning techniques such as deep learning algorithms have been harnessed to process various biosignals like EMG [70], [71], EEG [72], [73], and MRCP [37], [74]. While such techniques often achieve high performance, the high dimensionality of these models makes it challenging to identify key features and interpret the results neurophysiologically. Moreover, complex models require a large

volume of training datasets, which may not always be feasible, particularly for bio-signals. This study shows that using a minimal, neurophysiologically meaningful MRCP feature set provides adequate information about the kinetic output and enables successful classification of the response with up to four levels of intensity. This finding is significant because it demonstrates that relatively low-dimensional feature sets can help with the interpretability of results, especially when identifying motor impairments.

E. Potential of MRCP-Based Neurorehabilitation

The illustrated relationship between MRCP and RFD has significant potential for application to neurorehabilitation and HMI by providing information about the patient's intended kinetic parameters (i.e., force and especially RFD), so that the assistance can be tailored to the patient's intended task speed. We have shown that four levels of RFD can be most accurately classified when considering features at and following the movement onset (Fig. 8, Table III). The MRCP seems most suited for assistive BCI where the movement prediction can be ongoing while the subject attempts the task [75], [76]. By utilizing the post-movement discriminative power of the MRCP in conjunction with intention-detection algorithms [30], [32], [35], there is potential for new BCI technologies to determine the required assistive RFD for patients with sensorimotor impairments, improving the quality of neurorehabilitation. Additionally, the MRCP can be employed to trigger stimulation at approximately the movement onset and prompt neuroplastic changes in the nervous system [6], [34], [77]. The separation between Slow and Ballistic RFD by MRCP features at or before the movement onset (Fig. 4) shows the potential for adjusting stimulation in proportion to the classified level of RFD. Notably, the MRCP has been identified as a biomarker of stroke [78]. Therefore, the novel MRCP features discovered here can help enhance this biomarker's ability to differentiate impairments and motor improvements.

F. Limitations

One limitation of this study is that source localization was not performed on the EEG. The features pertaining to MRCP deflections before the start of the task (RP1 slope, RP2 slope, and $\min_1$) are components of motor preparation and likely to originate from the PMd [21], [27]. The rest of the waveform may represent mixed activity from the primary motor cortex, SMA, and other neighboring motor cortices [21], [79]. Another limitation is the number of subjects.

G. Future Work

Future works with a larger sample size can help to support the results of this study regarding the statistical and machine learning analysis. Future studies can also investigate RFD prediction from MRCP features when combining all subject trials and perhaps evaluate the model performance with leave-one-subject-out cross-validation [80], [81]. Previous works have shown that the MRCP amplitude is reduced in response to fatigue [82],

[83]. Future research can investigate the influence of fatigue on the proportionality between MRCP and RFD level that was demonstrated here.

V. CONCLUSION

In this paper, four RFD levels were successfully classified based on the MRCP. We found that the user's intended RFD level could be successfully decoded by features derived from (i) full-band EEG spanning nine electrodes with a classification accuracy of 83%, and (ii) the δ-band at Cz with a classification accuracy of 78%. The findings validated both hypotheses of the study, and show promise for decoding the user's intention from EEG with enhanced resolution. Key MRCP characteristics responded to the task intensity in an intuitive manner. Moreover, δ-band features showed high effect size and monotonic changes across the four RFD levels. The monotonic response and high classification accuracy show potential for mapping the MRCP to the user's intended RFD level. The relationship between MRCP and RFD could be harnessed in assistive technologies by allowing the patient to control the level of assistance based on their intended intensity.

Disclaimer: This article reflects the views of the authors and should not be construed to represent FDA's views or policies. The mention of commercial products, their sources, or their use in connection with material reported herein is not to be construed as either an actual or implied endorsement of such products by the Department of Health and Human Services.

REFERENCES

[1] R. Shadmehr and J. W. Krakauer, "A computational neuroanatomy for motor control," *Exp. Brain Res.*, vol. 185, no. 3, pp. 359–381, Mar. 2008.

[2] R. Shadmehr and H. H. Holcomb, "Neural correlates of motor memory consolidation," *Science*, vol. 277, no. 5327, pp. 821–825, Aug. 1997.

[3] H. Li et al., "EEG changes in time and Time-Frequency domain during movement preparation and execution in stroke patients," *Front. Neurosci.*, vol. 14, 2020, Art. no. 827.

[4] T. Hülsdünker et al., "Higher balance task demands are associated with an increase in individual alpha peak frequency," *Front. Hum. Neurosci.*, vol. 9, 2015, Art. no. 695.

[5] K. R. Ridderinkhof et al., "The role of the medial frontal cortex in cognitive control," *Science*, vol. 306, no. 5695, pp. 443–447, Oct. 2004.

[6] N. Mrachacz-Kersting et al., "Towards a mechanistic approach for the development of non-invasive brain-computer interfaces for motor rehabilitation," *J. Physiol.*, vol. 599, no. 9, pp. 2361–2374, May 2021.

[7] P. Cisek and J. F. Kalaska, "Neural correlates of reaching decisions in dorsal premotor cortex: Specification of multiple direction choices and final selection of action," *Neuron*, vol. 45, no. 5, pp. 801–814, Mar. 2005.

[8] Y. Nakayama et al., "Transformation of a virtual action plan into a motor plan in the premotor cortex," *J. Neurosci.*, vol. 28, no. 41, pp. 10287–10297, Oct. 2008.

[9] A. Pastor-Bernier et al., "Dorsal premotor cortex is involved in switching motor plans," *Front. Neuroeng.*, vol. 5, Apr. 2012, Art. no. 5.

[10] S. M. Peterson and D. P. Ferris, "Group-level cortical and muscular connectivity during perturbations to walking and standing balance," *Neuroimage*, vol. 198, pp. 93–103, Sep. 2019.

[11] A. Zénon et al., "Disrupting the supplementary motor area makes physical effort appear less effortful," *J. Neurosci.*, vol. 35, no. 23, pp. 8737–8744, Jun. 2015.

[12] A. Marlin et al., "Localizing evoked cortical activity associated with balance reactions: Does the anterior cingulate play a role," *J. Neurophysiol.*, vol. 111, no. 12, pp. 2634–2643, Jun. 2014.

[13] A. M. Payne and L. H. Ting, "Worse balance is associated with larger perturbation-evoked cortical responses in healthy young adults," *Gait Posture*, vol. 80, pp. 324–330, Jul. 2020.

[14] A. Mierau et al., "Changes in cortical activity associated with adaptive behavior during repeated balance perturbation of unpredictable timing," *Front. Behav. Neurosci.*, vol. 9, Oct. 2015, Art. no. 272.

[15] J. Ibáñez et al., "Low latency estimation of motor intentions to assist reaching movements along multiple sessions in chronic stroke patients: A feasibility study," *Front. Neurosci.*, vol. 11, Mar. 2017, Art. no. 126.

[16] K. Oh et al., "Improved cortical activity and reduced gait asymmetry during poststroke self-paced walking rehabilitation," *J. Neuroeng. Rehabil.*, vol. 18, no. 1, Apr. 2021, Art. no. 60.

[17] M. Butt et al., "Effect of Post-Stroke motor training on EEG Movement-Related cortical potentials," *J. NeuroEngineering Rehabil.*, 2020.

[18] C. Neuper et al., "Motor imagery and action observation: Modulation of sensorimotor brain rhythms during mental control of a brain–computer interface," *Clin. Neurophysiol.*, vol. 120, no. 2, pp. 239–247, Feb. 2009.

[19] O. Bai et al., "A high performance sensorimotor beta rhythm-based brain–computer interface associated with human natural motor behavior," *J. Neural Eng.*, vol. 5, no. 1, Dec. 2007, Art. no. 24.

[20] M.-K. Lu et al., "Movement related cortical potentials of cued versus self-initiated movements: Double dissociated modulation by dorsal premotor cortex versus supplementary motor area rTMS," *Hum. Brain Mapping*, vol. 33, no. 4, pp. 824–839, Apr. 2012.

[21] N. Mrachacz-Kersting et al., "Precise temporal association between cortical potentials evoked by motor imagination and afference induces cortical plasticity," *J. Physiol.*, vol. 590, no. 7, pp. 1669–1682, Apr. 2012.

[22] S. M. Slobounov and W. J. Ray, "Movement-related potentials with reference to isometric force output in discrete and repetitive tasks," *Exp. Brain Res.*, vol. 123, no. 4, pp. 461–473, Dec. 1998.

[23] O. F. do Nascimento et al., "Relationship between plantar-flexor torque generation and the magnitude of the movement-related potentials," *Exp. Brain Res.*, vol. 160, no. 2, pp. 154–165, Jan. 2005.

[24] S. Olsen et al., "Electroencephalographic recording of the movement-related cortical potential in ecologically valid movements: A scoping review," *Front. Neurosci.*, vol. 15, Sep. 2021, Art. no. 721387.

[25] M. Jochumsen and I. K. Niazi, "Detection and classification of single-trial movement-related cortical potentials associated with functional lower limb movements," *J. Neural Eng.*, vol. 17, no. 3, Jul. 2020, Art. no. 035009.

[26] D. J. Wright et al., "Using the movement-related cortical potential to study motor skill learning," *J. Motor Behav.*, vol. 43, no. 3, pp. 193–201, 2011.

[27] A. Shakeel et al., "A review of techniques for detection of movement intention using Movement-related cortical potentials," *Comput. Math. Methods Med.*, vol. 2015, pp. 1–13, 2015.

[28] V. Siemionow et al., "Relationship between motor activity-related cortical potential and voluntary muscle activation," *Exp. Brain Res.*, vol. 133, no. 3, pp. 303–311, Aug. 2000.

[29] O. F. do Nascimento et al., "Movement-related parameters modulate cortical activity during imaginary isometric plantar-flexions," *Exp. Brain Res.*, vol. 171, no. 1, pp. 78–90, May 2006.

[30] D. Farina et al., "Movement-Related cortical potentials and their application in Brain-Computer interfacing," in *Proc. Introduction Neural Eng. Motor Rehabil.*, 2013, pp. 253–266.

[31] H. Shibasaki and M. Hallett, "What is the bereitschaftspotential," *Clin. Neurophysiol.*, vol. 117, no. 11, pp. 2341–2356, 2006.

[32] Y. Gu et al., "Comparison of movement related cortical potential in healthy people and amyotrophic lateral sclerosis patients," *Front. Neurosci.*, vol. 7, May 2013, Art. no. 65.

[33] J. Ibáñez, J. I. Serrano, M. D. del Castillo, and L. J. Barrios, "An asynchronous BMI system for online single-trial detection of movement intention," in *Proc. IEEE Annu. Int. Conf. Eng. Med. Biol.*, 2010, pp. 4562–4565.

[34] I. K. Niazi, N. Mrachacz-Kersting, N. Jiang, K. Dremstrup, and D. Farina, "Peripheral electrical stimulation triggered by self-paced detection of motor intention enhances motor evoked potentials," *IEEE Trans. Neural Syst. Rehabil. Eng.*, vol. 20, no. 4, pp. 595–604, Jul. 2012.

[35] F. Karimi et al., "Detection of movement related cortical potentials from EEG using constrained ICA for Brain-Computer interface applications," *Front. Neurosci.*, vol. 11, 2017, Art. no. 356.

[36] M. Jochumsen et al., "Detection and classification of movement-related cortical potentials associated with task force and speed," *J. Neural Eng.*, vol. 10, no. 5, Oct. 2013, Art. no. 056015.

[37] R. Gatti et al., "Convolutional neural networks improve the prediction of hand movement speed and force from single-trial EEG," *bioRxiv*, 2019. [Online]. Available: https://www.biorxiv.org/content/early/2019/05/22/492660

[38] R. Xu, N. Jiang, C. Lin, N. Mrachacz-Kersting, K. Dremstrup, and D. Farina, "Enhanced low-latency detection of motor intention from EEG for closed-loop Brain-Computer interface applications," *IEEE Trans. Biomed. Eng.*, vol. 61, no. 2, pp. 288–296, Feb. 2014.

[39] K. Wang et al., "Enhance decoding of pre-movement EEG patterns for brain computer interfaces," *J. Neural Eng.*, vol. 17, no. 1, Jan. 2020, Art. no. 016033.

[40] M. H. Alomari et al., "Automated classification of L/R hand movement EEG signals using advanced feature extraction and machine learning," *Int. J. Adv. Comput. Sci. Appl.*, vol. 4, no. 6,2013.

[41] Y. Gu et al., "Identification of task parameters from movement-related cortical potentials," *Med. Biol. Eng. Comput.*, vol. 47, no. 12, pp. 1257–1264, Dec. 2009.

[42] A. Mognon et al., "ADJUST: An automatic EEG artifact detector based on the joint use of spatial and temporal features," *Psychophysiol.*, vol. 48, no. 2, pp. 229–240, 2011.

[43] S. Aliakbaryhosseinabadi et al., "Detection of movement intention from movement-related cortical potentials with different paradigms," in *Proc. Biosyst. Biorobotics*, 2014, pp. 237–244.

[44] J. N. Acharya et al., "American clinical neurophysiology society guideline 2: Guidelines for standard electrode position nomenclature," *J. Clin. Neurophysiol.*, vol. 33, no. 4, pp. 308–311, Aug. 2016.

[45] C. Carvalhaes and J. A. de Barros, "The surface Laplacian technique in EEG: Theory and methods," *Int. J. Psychophysiol.*, vol. 97, no. 3, pp. 174–188, 2015.

[46] G. Li et al., "A novel feature extraction method for machine learning based on surface electromyography from healthy brain," *Neural Comput. Appl.*, vol. 31, no. 12, pp. 9013–9022, Dec. 2019.

[47] A. Waris and E. N. Kamavuako, "Effect of threshold values on the combination of EMG time domain features: Surface versus intramuscular EMG," *Biomed. Signal Process. Control*, vol. 45, pp. 267–273, Aug. 2018.

[48] M. Borowska, "Entropy-based algorithms in the analysis of biomedical signals," *Stud. Logic, Grammar Rhetoric*, vol. 43, no. 1, pp. 21–32, Dec. 2015.

[49] J. Gao et al., "Entropy measures for biological signal analyses," *Nonlinear Dyn.*, vol. 68, no. 3, pp. 431–444, May 2012.

[50] D. Freedman and P. Diaconis, "On the histogram as a density estimator:l 2 theory," *Z. Wahrscheinlichkeitstheorie verw Gebiete*, vol. 57, no. 4, pp. 453–476, Dec. 1981.

[51] H. J. Keselman et al., "The analysis of repeated measures designs: A review," *Brit. J. Math. Statist. Psychol.*, vol. 54, no. Pt 1, pp. 1–20, May 2001.

[52] J. Dien and A. M. Santuzzi, "Application of repeated measures ANOVA to high-density ERP datasets: A review and tutorial," in *Event-Related Potentials: A Methods Handbook*, Cambridge, MA, USA: MIT Press, 2005, pp. 57–82.

[53] J. L. Hodges and E. L. Lehmann, "Rank methods for combination of independent experiments in analysis of variance," in *Selected Works of E. L. Lehmann, J. Rojo, Ed.* Boston, MA: Berlin, Germany: Springer, 2012, pp. 403–418.

[54] J. O. Wobbrock et al., "The aligned rank transform for nonparametric factorial analyses using only anova procedures," in *Proc. SIGCHI Conf. Hum. Factors Comput. Syst.*, New York, NY, USA, 2011, pp. 143–146.

[55] L. N. Muhammad, "Guidelines for repeated measures statistical analysis approaches with basic science research considerations," *J. Clin. Invest.*, vol. 133, no. 11, Jun. 2023, Art. no.e171058.

[56] H. Abdi, "Holm's sequential bonferroni procedure," *Encyclopedia Res. Des.*, vol. 1, no. 8, pp. 1–8, 2010.

[57] S. Olejnik et al., "Multiple testing and statistical power with modified Bonferroni procedures," *J. Educ. Behav. Stat.*, vol. 22, no. 4, pp. 389–406, Dec. 1997.

[58] A. M. Maitín et al., "Machine learning approaches for detecting Parkinson's disease from EEG analysis: A systematic review," *Appl. Sci*, vol. 10, 2020, Art. no. 8662.

[59] D. Pathak et al., "Chapter 10-A study of deep learning approach for the classification of electroencephalogram (EEG) brain signals," in *Artificial Intelligence and Machine Learning for EDGE Computing*, R. Pandey et al., Eds. San Francisco, CA, USA: Academic, 2022, pp. 133–144.

[60] B. T. Volpe et al., "A novel approach to stroke rehabilitation," *Neurology*, vol. 54, no. 10, pp. 1938–1944, 2000.

[61] N. Takeuchi and S.-I. Izumi, "Rehabilitation with poststroke motor recovery: A review with a focus on neural plasticity," *Stroke Res. Treat.*, vol. 2013, pp. 128641–128641, 2013.

[62] M. Jochumsen et al., "Comparison of spatial filters and features for the detection and classification of movement-related cortical potentials in

healthy individuals and stroke patients," *J. Neural Eng.*, vol. 12, no. 5, Jul. 2015, Art. no. 056003.

[63] M. Jochumsen et al., "Detecting and classifying movement-related cortical potentials associated with hand movements in healthy subjects and stroke patients from single-electrode, single-trial EEG," *J. Neural Eng.*, vol. 12, no. 5, Aug. 2015, Art. no. 056013.

[64] U. Rashid, I. K. Niazi, M. Jochumsen, L. R. Krol, N. Signal, and D. Taylor, "Automated labeling of movement- related cortical potentials using segmented regression," *IEEE Trans. Neural Syst. Rehabil. Eng.*, vol. 27, no. 6, pp. 1282–1291, Jun. 2019.

[65] J. A. Palmer et al., "Prefrontal-motor and somatosensory-motor cortical network interactions during reactive balance are associated with distinct aspects of balance behavior in older adults," Feb. 2021. [Online]. Available: https://www.biorxiv.org/content/biorxiv/early/2021/02/01/2021.01.30.428951

[66] J. Wagner et al., "Trial-by-trial source-resolved EEG responses to gait task challenges predict subsequent step adaptation," *Neuroimage*, vol. 199, pp. 691–703, Oct. 2019.

[67] S. Slobounov et al., "Perceived effort in force production as reflected in motor-related cortical potentials," *Clin. Neurophysiol.*, vol. 115, no. 10, pp. 2391–2402, 2004.

[68] J. Ibáñez et al., "Detection of the onset of upper-limb movements based on the combined analysis of changes in the sensorimotor rhythms and slow cortical potentials," *J. Neural Eng.*, vol. 11, no. 5, Aug. 2014, Art. no. 056009.

[69] E. A. Zeid et al., "A pipeline of spatio-temporal filtering for predicting the laterality of self-initiated fine movements from single trial readiness potentials," *J. Neural Eng.*, vol. 13, no. 6, Dec. 2016, Art. no. 066012.

[70] P. Xia et al., "EMG-based estimation of limb movement using deep learning with recurrent convolutional neural networks," *Artif. Organs*, vol. 42, no. 5, pp. E67–E77, May 2018.

[71] A. K. Clarke et al., "Deep learning for robust decomposition of High-Density surface EMG signals," *IEEE Trans. Biomed. Eng.*, vol. 68, no. 2, pp. 526–534, Feb. 2021.

[72] R. T. Schirrmeister et al., "Deep learning with convolutional neural networks for EEG decoding and visualization," *Hum. Brain Mapping*, vol. 38, no. 11, pp. 5391–5420, Nov. 2017.

[73] A. Craik et al., "Deep learning for electroencephalogram (EEG) classification tasks: A review," *J. Neural Eng.*, vol. 16, no. 3, Jun. 2019, Art. no. 031001.

[74] V. J. Lawhern et al., "EEGNet: A compact convolutional neural network for EEG-based brain–computer interfaces," *J. Neural Eng.*, vol. 15, no. 5, Jul. 2018, Art. no. 056013.

[75] I. K. Niazi et al., "Detection of movement intention from single-trial movement-related cortical potentials," *J. Neural Eng.*, vol. 8, no. 6, Dec. 2011, Art. no. 066009.

[76] F. Cincotti et al., "Non-invasive brain–computer interface system: Towards its application as assistive technology," *Brain Res. Bull.*, vol. 75, no. 6, pp. 796–803, 2008.

[77] N. Mrachacz-Kersting et al., "Efficient neuroplasticity induction in chronic stroke patients by an associative brain-computer interface," *J. Neurophysiol.*, vol. 115, no. 3, pp. 1410–1421, Mar. 2016.

[78] L. Chen et al., "Assessing the relationship between motor anticipation and cortical excitability in subacute stroke patients with Movement-Related potentials," *Front. Neurol.*, vol. 9, Oct. 2018, Art. no. 881.

[79] T. Hamano et al., "The cortical generators of the contingent negative variation in humans: A study with subdural electrodes," *Electroencephalogr. Clin. Neurophysiol.*, vol. 104, no. 3, pp. 257–268, May 1997.

[80] S. Kunjan et al., "The necessity of leave one subject out (LOSO) cross validation for EEG disease diagnosis," in *Brain Informatics*. Berlin, Germany: Springer, 2021, pp. 558–567.

[81] Y. Roy et al., "Deep learning-based electroencephalography analysis: A systematic review," *J. Neural Eng.*, vol. 16, no. 5, Aug. 2019, Art. no. 051001.

[82] G. Dirnberger et al., "Fatigue in a simple repetitive motor task: A combined electrophysiological and neuropsychological study," *Brain Res.*, vol. 1028, no. 1, pp. 26–30, Nov. 2004.

[83] F. Guo et al., "Perceived exertion during muscle fatigue as reflected in movement-related cortical potentials: An event-related potential study," *Neuroreport*, vol. 28, no. 3, pp. 115–122, Feb. 2017.